



Cite this: *J. Mater. Chem. A*, 2014, 2, 18367

In situ synthesis of SnO₂ nanoparticles encapsulated in micro/mesoporous carbon foam as a high-performance anode material for lithium ion batteries†

Xiulin Fan,^{ab} Jie Shao,^a Xuezhong Xiao,^a Xinhua Wang,^a Shouquan Li,^a Hongwei Ge,^a Lixin Chen^{*a} and Chunsheng Wang^{*b}

SnO₂ has high capacity but poor cycling stability for Li-ion batteries due to pulverization and aggregation. Herein, we tackle these two challenges by uniformly dispersing carbon coated nano-SnO₂ into a micro-sized porous carbon matrix to form a nano-SnO₂/C composite anode using a facile and scalable *in situ* synthesis strategy. The SnO₂@C nanocomposite exhibits a capacity of 640 mA h g⁻¹ at 500 mA g⁻¹ in the initial 150 cycles and then increases to 720 mA h g⁻¹ and maintains this capacity for 420 cycles. The superior electrochemical performance with long cycle lifetimes of the carbon foam–SnO₂ nanocomposites could be attributed to their unique carbon microstructures: the network of carbon sheets provides favorable electron transport, while the interconnected micro-/mesopores can serve as the effective channels of lithium ion transport, thereby supplying short lithium ion diffusion pathways. Meanwhile, these pores surrounding the active species of nano-SnO₂ along with flexible carbon nanosheets can accommodate the severe volume variations during prolonged electrochemical cycling and mitigate the Sn aggregation. The present study provides a large-scale synthesis route to synthesize SnO₂-based anode materials with superior electrochemical performance for lithium ion batteries.

Received 18th August 2014
Accepted 9th September 2014

DOI: 10.1039/c4ta04278f

www.rsc.org/MaterialsA

Introduction

Rechargeable lithium ion batteries (LIBs) have been extensively employed as energy sources for portable electronic devices¹ and are now showing promising applications in electric vehicles and grid energy storage.^{2,3} As promising anode materials, tin-based compounds have been extensively investigated due to their high theoretical capacities and low voltage plateau *vs.* Li⁺/Li.^{4–6} Among them, SnO₂ is considered to be the most attractive anode material due to its high theoretical capacity of 790 mA h g⁻¹.⁷ However, the poor cycling performance caused by serious Sn particle aggregation and considerable volume change upon cycling hampers its industrial applications.⁸ Besides, the intrinsic low electrical conductivity of SnO₂ also reduces the rate

performance. Several strategies have been reported to circumvent these intractable issues. One effective protocol is to design SnO₂ nanomaterials with different morphologies ranging from 1D nanorods to 3D nanostructures,^{9–14} which can effectively sustain the volume variation, and more effectively access to Li⁺ ions in the electrolytes.¹⁵ Another useful approach is to construct SnO₂ nanocomposites with conducting materials such as amorphous carbon,^{16–18} graphene,^{19–26} carbon tubes,²⁷ graphite^{28–30} and conducting polymers³¹ to improve the conductivity of SnO₂ anodes, circumvent the aggregation and pulverization of Sn nanoparticles. Sun *et al.*³² deposited the SnO₂ nanoparticles onto the graphene nanosheets using the atomic layer deposition (ALD) method. Wang *et al.*³³ fabricated graphene–SnO₂ sandwich structures, using GO and SnCl₂ as the precursors. Using the hard template method, Lou *et al.*¹⁸ designed a coaxial SnO₂@carbon hollow sphere. These SnO₂/carbon composites with precisely controlled structure exhibit a high capacity and long cycling life. However, complex and expensive synthesis methods limit wide applications of these materials. To reduce the cost, Wang *et al.*³⁴ fabricated the SnO₂@C composite by a simple impregnation–calcination method, but the SnO₂@C composite provides a capacity of 730 mA h g⁻¹ in the 10th cycle and quickly drops to 590 mA h g⁻¹ in the 50th cycle. More recently, Jahel *et al.*³⁵ synthesized a micro/mesoporous SnO₂/C composite by impregnating tin salt

^aState Key Laboratory of Silicon Materials, Key Laboratory of Advanced Materials and Application for Batteries of Zhejiang Province, Department of Materials Science and Engineering, Zhejiang University, Hangzhou 310027, PR China. E-mail: lxchen@zju.edu.cn; Fax: +86 571 87951152; Tel: +86 571 87951152

^bDepartment of Chemical and Biomolecular Engineering, University of Maryland, College Park, MD 20742, USA. E-mail: cswang@umd.edu

† Electronic supplementary information (ESI) available: A thermogravimetric (TGA) profile of the SnO₂@C porous composite, a TEM image of the SnO₂@C porous composite after being ultrasonicated in ethanol for up to 6 h, and galvanostatic charge–discharge profiles of the mixture of commercial SnO₂ nanoparticles and carbon black electrodes at a constant current density of 500 mA g⁻¹. See DOI: 10.1039/c4ta04278f

solution into the porous carbon. The composite was reported to possess a reversible initial capacity of 916 mA h g^{-1} , but the capacity drops to maintain 560 mA h g^{-1} after 100 cycles at a rate of 1 C. The SnO_2/C composites synthesized using facile methods show unsatisfactory cycling stability due to their inhomogeneous structure. The synthesis of a SnO_2 -based electrode with superior lithium storage performance using a scalable and facile method still remains a significant challenge.³⁶ The ease of fabrication of electrode materials that can be mass produced at low cost is of great interest on an industrial scale.³⁷

In this study, $\text{SnO}_2@\text{C}$ nanocomposites with superior electrochemical performance were synthesized using a facile and scalable solution–evaporation–calcination method (Scheme 1). The *in situ* synthesized composite exhibits a high capacity of 420 mA h g^{-1} at 2000 mA g^{-1} and maintains 720 mA h g^{-1} at 500 mA g^{-1} for 420 cycles, which is similar to or better than the SnO_2/C composite synthesized using very expensive soft^{34,35,38} or hard template methods.³⁹ The exceptional performance of the $\text{SnO}_2@\text{C}$ nanocomposite is attributed to the unique structure. In the $\text{SnO}_2@\text{C}$ nanocomposite, SnO_2 nanoparticles uniformly dispersed in the micro/mesoporous carbon matrix, where the porous carbon can effectively accommodate the volume change of SnO_2 during lithiation/delithiation, quickly transport the electrons and Li-ions, and mitigate the nano-Sn aggregation.

Experimental section

Material synthesis

Stannous sulfate (SnSO_4), sodium sulfate (Na_2SO_4), sulfuric acid (H_2SO_4) and sucrose ($\text{C}_{12}\text{H}_{22}\text{O}_{11}$) were purchased from Sino-pharm Chemical Reagent Co., Ltd. SnO_2 nanoparticles ($\sim 50 \text{ nm}$) were purchased from Aladdin Co. Ltd. All reagents were of analytical grade and used as received without any further purification. To prepare the carbon foam–nano SnO_2 composite, SnSO_4 (12 g), carbon precursor of sucrose (12 g), and the dispersant Na_2SO_4 (24 g) were dissolved in 100 mL of deionized water. Sulfuric acid (2 mL) was added to the solution to suppress the hydrolysis of SnSO_4 and catalyze the carbonization of sucrose. The resulting mixed solution was dried in a drying oven under severe stirring, followed by ball milling for 20 min to obtain very fine powder. After that, the powder was calcined at 400°C for 2 h and subsequently at 600°C for 4 h in a tube furnace under an Ar atmosphere and then cooled to room temperature in the presence of Ar. The obtained black product was washed with deionized water several times to dissolve

Na_2SO_4 and then a pure carbon foam–nano SnO_2 ($\text{SnO}_2@\text{C}$) composite was obtained.

Characterization

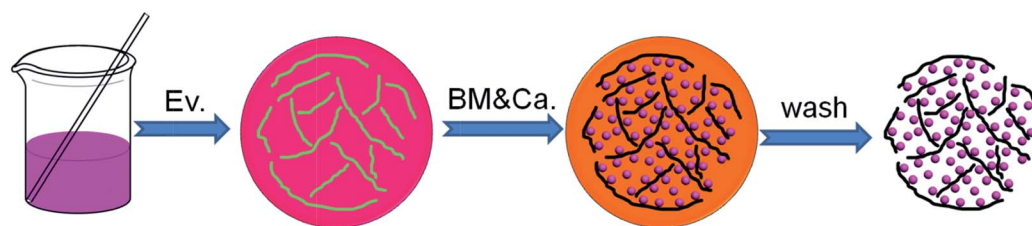
X-ray diffraction (XRD) experiments of the samples were performed on an X'Pert Pro X-ray diffractometer (PANalytical, the Netherlands) with $\text{Cu K}\alpha$ radiation at 40 kV and 40 mA. X-ray photoelectron spectroscopy (XPS) was carried out on a VG ESCALAB MARK II system with $\text{Mg K}\alpha$ radiation (1253.6 eV) at a base pressure of 1×10^{-8} Torr. All binding energy values were referenced to the C 1s peak of carbon at 284.6 eV with an uncertainty of $\pm 0.2 \text{ eV}$. Transmission electron microscopy (TEM, Tecnai G2 F30) and scanning electron microscopy (SEM, Hitachi SU-70) were performed to examine the morphology and microstructure of the products. Pore size distributions, specific surface areas and pore volumes of the samples were characterized by N_2 adsorption by means of a Quantacrome Autosorb-1-C system using the Brunauer–Emmett–Teller (BET) and Barrett–Joyner–Halenda (BJH) methods.

Electrochemical investigation

The electrochemical tests were performed using a coin-type half cell (CR 2025). Metallic lithium was used as the negative electrode. To prepare working electrodes, $\text{SnO}_2@\text{C}$ or nano SnO_2 –CB mixture (70 : 25), carbon black (CB), styrene–butadiene rubber (SBR) and sodium carboxymethyl cellulose (CMC) with a mass ratio of 90 : 5 : 2.5 : 2.5 were mixed into a homogeneous slurry in deionized water with a pestle and mortar. The slurry mixture was coated onto Cu foil and then dried at 80°C for 12 h under vacuum. The electrolyte solution was comprised of 1 M LiPF_6 in ethylene carbonate (EC)/dimethyl carbonate (DMC)/ethylmethyl carbonate (EMC) (1 : 1 : 1 by volume). The cells were assembled with a polypropylene (PP) microporous film (Celgard 2300) as the separator. Charge–discharge experiments were performed at a constant current density between 0.005 and 3 V using a LAND CT2001A Battery Cycler at room temperature. Cyclic voltammetry (CV) was performed on the CHI660E electrochemical workstation in the potential range of 0–3.0 V (vs. Li^+/Li) at a scan rate of 0.1 mV s^{-1} .

Results and discussion

In the present work, using SnSO_4 as a SnO_2 source and sucrose as carbon sources, and Na_2SO_4 as a dispersant, a facile solution-



Scheme 1 Schematic illustration of the formation process of the $\text{SnO}_2@\text{C}$ porous composite. Ev., BM and Ca. denote evaporation, ball milling and calcination, respectively.

evaporation–calcination method is used to *in situ* synthesize the $\text{SnO}_2\text{@C}$ porous composite. The strategy for synthesizing the $\text{SnO}_2\text{@C}$ composite is schematically depicted in Scheme 1. The detailed procedures are shown in the Experimental section. First, SnSO_4 , NaSO_4 and sucrose are dissolved in water to form a solution and then evaporated. During the evaporation of the solution, the sucrose will be polymerized into a polymerization network in the presence of sulfuric acid. At the same time, the hydrolysis of SnSO_4 is suppressed by the sulfuric acid, resulting in a homogeneous dispersion of sulfate in the polymerization network. In the subsequent calcination, SnSO_4 decomposes into SnO_2 nanocrystals and the polymerization network carbonizes into carbon nanosheets. The presence of Na_2SO_4 can separate SnSO_4 and therefore suppress the overgrowth of SnO_2 nanoparticles during SnSO_4 decomposition. Ten grams of the composite can be prepared in a batch, and Na_2SO_4 can be collected and reused after crystallization. The uniformly distributed pores formed during the removal of Na_2SO_4 can effectively accommodate the volume change, and accelerate ion diffusion in the $\text{SnO}_2\text{@C}$ electrode during lithiation/delithiation processes.

The phases of the $\text{SnO}_2\text{@C}$ porous composite were characterized by XRD. For comparison, the pattern of the commercial nano- SnO_2 (~ 50 nm) is also shown. Fig. 1 shows the XRD patterns of the $\text{SnO}_2\text{@C}$ porous composite and commercial nano- SnO_2 . All peaks in the XRD patterns of the composite can be indexed to tetragonal SnO_2 (JCPDS no. 41-1445). Compared to the XRD patterns of the commercial nano- SnO_2 samples, the wide diffraction peaks of the $\text{SnO}_2\text{@C}$ nanocomposites may be attributed to the small SnO_2 particle sizes. The average grain size of SnO_2 nanoparticles in the composites is calculated from the three largest diffraction peaks (110), (101) and (211) by using the Scherrer equation ($d = 0.9\lambda/\beta \cos \theta$), and the estimated average crystal size is about 14.5 nm for SnO_2 nanoparticles.

The carbon content in $\text{SnO}_2\text{@C}$ nanocomposites was determined using thermogravimetric analysis (TGA) (Fig. S1†). The fraction of nano- SnO_2 in the composite is calculated to be 71.1%

by weight. The SnO_2 percentage of the composite is higher than that of most of the composites synthesized by impregnation methods,^{27,35} which ensures a higher reversible capacity for the composite.

The morphology of the $\text{SnO}_2\text{@C}$ composite was studied using transmission electron microscopy (TEM, Fig. 2a–c), scanning electron microscopy (SEM, Fig. 2d and e) and high resolution transmission electron microscopy (HRTEM, Fig. 2f). As shown in Fig. 2a, typical $\text{SnO}_2\text{@C}$ porous particles are in micro-size with a diameter of 1.5 μm . In the magnified TEM images (Fig. 2b and c), SnO_2 nanoparticles are uniformly distributed and entangled in the micro-sized carbon matrix. The carbon matrix is composed of carbon nanosheets, which can be clearly observed in Fig. 2a, b and e, denoted as CS in the figure. From Fig. 2a, b and e, it can be clearly seen that the nanoparticles of SnO_2 are totally blanketed and separated by the carbon sheets. The HRTEM image (Fig. 2f) demonstrates that the SnO_2 nanoparticles are in a single crystal with a size of 10–20 nm, which is consistent with the XRD results. Lattice fringes with a spacing of 0.26 nm can be seen from the HRTEM image, corresponding to the (101) planes of SnO_2 . It is worth noting that no visible change can be observed after ultrasonication of the dispersion solution of the $\text{SnO}_2\text{@C}$ composite in ethanol for up to 6 h (Fig. S2†), which demonstrates the strong interaction between the SnO_2 and carbon sheets. The strong interaction between SnO_2 and carbon will greatly enhance the charge–discharge cycling stability.

Compared to 2D composites, such as nanosheet supported materials,^{40,41} 3D nanoporous $\text{SnO}_2\text{@C}$ composite particles with micro-size can better accommodate the volume change and refrain the cracking, crumbling and SnO_2 pulverization because the carbon matrix with layers of carbon sheets can safeguard the *in situ* formed nano- SnO_2 in all directions. In the case of two dimensional composites, the amorphous alloy aggregates generated after lithiation are easily peeled off from the surface of the supporters upon cycling because of the weak contact between the particle and supporters, therefore leading to a fast decay of the electrode capacity.^{33,42}

The structures of $\text{SnO}_2\text{@C}$ nanoporous composites were further characterized using a surface-sensitive high-resolution X-ray photoelectron spectroscope (XPS).⁴³ Fig. 3 shows the typical full XPS spectra of the $\text{SnO}_2\text{@C}$ porous composite and commercial nano- SnO_2 . The photoelectron lines at a binding energy of about 285 and 532 eV observed both in the $\text{SnO}_2\text{@C}$ porous composite and commercial nano- SnO_2 are attributed to C 1s and O 1s, respectively. Intensive peaks of Sn 3d_{5/2} and 3d_{3/2} at ~ 487 and ~ 495 eV are clearly observed in commercial nano- SnO_2 nanoparticles,⁴⁴ but are almost absent for the $\text{SnO}_2\text{@C}$ porous composite. Since the atomic sensitivity factor of Sn is much higher than those of C and O,⁴⁵ the dramatic reduction in signals of Sn 3d_{5/2} and 3d_{3/2} implies that the *in situ* formed SnO_2 nanoparticles in the $\text{SnO}_2\text{@C}$ nanoporous composite are covered by carbon layers, which is in good agreement with the above SEM and TEM observations. The carbon layer coating on nano- SnO_2 can increase the electronic conductivity and prevent nano-Sn aggregations during repeated lithiation/delithiation.

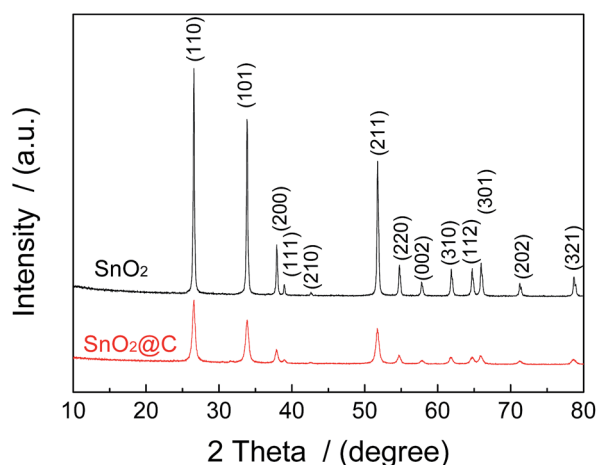


Fig. 1 XRD patterns of the as-synthesized $\text{SnO}_2\text{@C}$ composite and commercial SnO_2 nanoparticles.

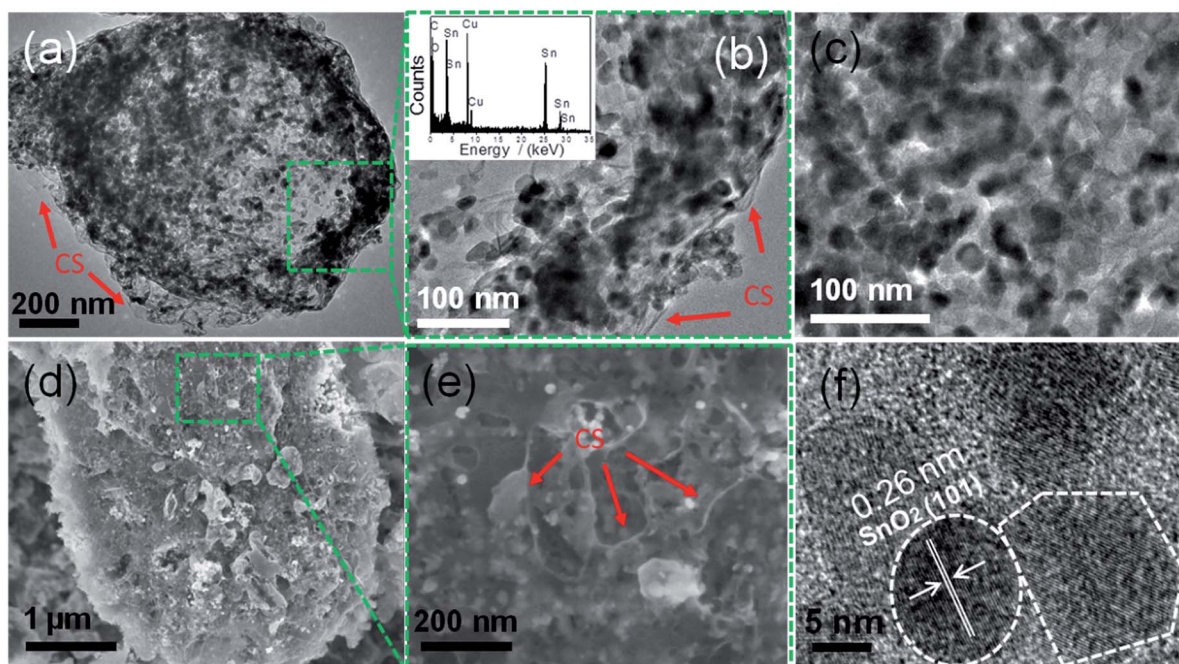


Fig. 2 (a) TEM image of the $\text{SnO}_2\text{@C}$ porous composite. (b) and (c) are the magnified images of the border and interior of the composite, respectively. The inset of (b) shows the EDS result of the composite. The presence of Cu is derived from the copper mesh that supports the carbon film with the sample during measurement. (d) and (e) are SEM images of the $\text{SnO}_2\text{@C}$ foam. (f) HRTEM image of the $\text{SnO}_2\text{@C}$ porous composite. CS denotes carbon sheets.

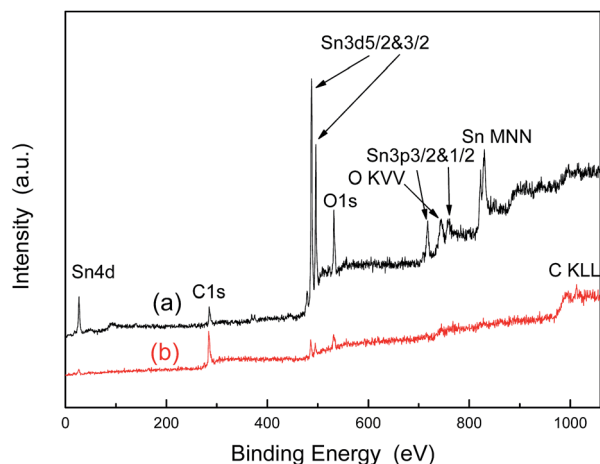


Fig. 3 XPS survey scans of (a) commercial SnO_2 nanoparticles and (b) as-prepared $\text{SnO}_2\text{@C}$ porous composite.

The porous structure of $\text{SnO}_2\text{@C}$ was determined by N_2 isothermal adsorption/desorption measurements. Fig. 4 depicts the N_2 adsorption/desorption isotherm of the composite and the corresponding pore size distribution determined by the Barrett-Joyner-Halenda (BJH) model (inset, Fig. 4). The BET specific surface area is measured to be $\sim 326 \text{ m}^2 \text{ g}^{-1}$, which is much higher than that of the composite synthesized by the impregnation method.³⁴ The large specific surface area would be beneficial to increase the contact with electrolyte and Li diffusion upon lithiation/delithiation. The pore size

distribution (inset of Fig. 4) shows that the composite exhibits a mixed micro-/mesoporous structure. The micropores may come from the carbonization of sucrose due to the release of volatile species,⁴⁶ while the mesopores arise from the dissolution of Na_2SO_4 after calcination. Based on the BET data, the specific pore volume of $\text{SnO}_2\text{@C}$ is calculated to be $0.65 \text{ cm}^3 \text{ g}^{-1}$. The mesopores associated with micropores can effectively accommodate the severe volume changes during electrochemical lithiation/delithiation processes, which would increase the general mechanical resistance of the composite matrix as a whole.

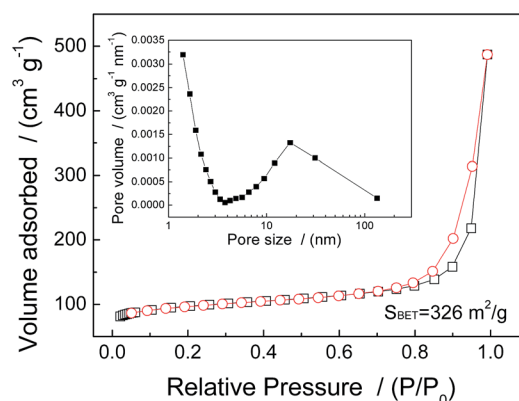


Fig. 4 N_2 adsorption/desorption isotherm of the $\text{SnO}_2\text{@C}$ porous composite; the inset is the BJH pore size distribution curve.

The electrochemical performance of the $\text{SnO}_2\text{@C}$ porous composite was evaluated using coin-type half cells and compared to that of commercial nano- SnO_2 . Fig. 5a shows the cyclic voltammetry (CV) curves of the $\text{SnO}_2\text{@C}$ electrode in the first six cycles between 0.005 and 3 V vs. Li^+/Li . A small lithiation (cathodic) shoulder at 0.7–0.95 V and a large peak at 0.1 V in the first cycle can be assigned to the irreversible formation of $\text{Li}_2\text{O}/\text{SEI}$ and a Li_xSn alloy, respectively. During the first delithiation (anodic) process, the strong peak at 0.7 V and the broad peak at 1.26 V correspond to the delithiation phase transition from the Li_xSn alloy to Sn .²⁵ The CV curves of the following cycles almost overlap, implying the excellent reversibility of the $\text{SnO}_2\text{@C}$ electrode. Fig. 5b shows the charge–discharge profiles of the

$\text{SnO}_2\text{@C}$ electrode at a current rate of 500 mA g^{-1} between 0.005 and 3 V. A delithiation plateau at 0.7 V is observed in the first discharge of commercial SnO_2 nanoparticles (Fig. S3†) and becomes a slope plateau at 0.7–0.5 V for the $\text{SnO}_2\text{@C}$ nanoporous composite (Fig. 5b), which is due to the formation of SEI and the conversion of SnO_2 to Li_2O and Sn .³³ This potential plateau is significantly reduced in the second lithiation, demonstrating the irreversible reaction of SEI formation and conversion reaction. The initial discharge and charge capacities of the $\text{SnO}_2\text{@C}$ composite are 1473 and 640 mA h g^{-1} with a coulombic efficiency of 43.4%. The relatively low initial coulombic efficiency is ascribed to the irreversible conversion of SnO_2 into Sn and Li_2O ,^{47,48} and the formation of SEI films^{49–51} with minor contribution from the irreversible insertion of Li^+ into the micropores in the carbon matrix.³⁵ The cycling performances of the $\text{SnO}_2\text{@C}$ composite and nano- SnO_2 are shown in Fig. 5c. The reversible capacity of the $\text{SnO}_2\text{@C}$ porous composite gradually increases from initial 640 mA h g^{-1} to more than 720 mA h g^{-1} at the 200th cycle, and maintain 720 mA h g^{-1} for 410 cycles. A volumetric capacity of $1100 \text{ mA h cm}^{-3}$ is achieved for $\text{SnO}_2\text{@C}$. The behavior of capacity increase has been reported for the Sn/C nanocomposite,^{38,52} SnO_2 nanocomposite⁵³ and other metal oxide systems,^{54,55} which can be attributed to the reversible formation and decomposition of an organic polymeric/gel-like layer from the electrolyte during discharge–charge cycling,⁵² or delithiation/lithiation of LiOH .⁵⁶ The coulombic efficiency increases from initial 43.4% to >99.5% in ten cycles and 99.5% of coulombic efficiency is maintained for 410 cycles. In contrast, the capacity of commercial nano- SnO_2 quickly drops from 650 mA h g^{-1} to 30 mA h g^{-1} in 40 cycles. The rapid capacity decline is also reported for many nano- SnO_2 materials.^{15,17,57,58}

The $\text{SnO}_2\text{@C}$ composite with the porous carbon matrix also exhibits much exceptional rate capability, as shown in Fig. 6. The $\text{SnO}_2\text{@C}$ porous composite can provide 730 mA h g^{-1} at 200 mA g^{-1} , 510 mA h g^{-1} at 1000 mA g^{-1} , 420 mA h g^{-1} at 2000 mA g^{-1} , and 250 mA h g^{-1} even at a current density of 4000 mA g^{-1} , which is one of the best performances among the

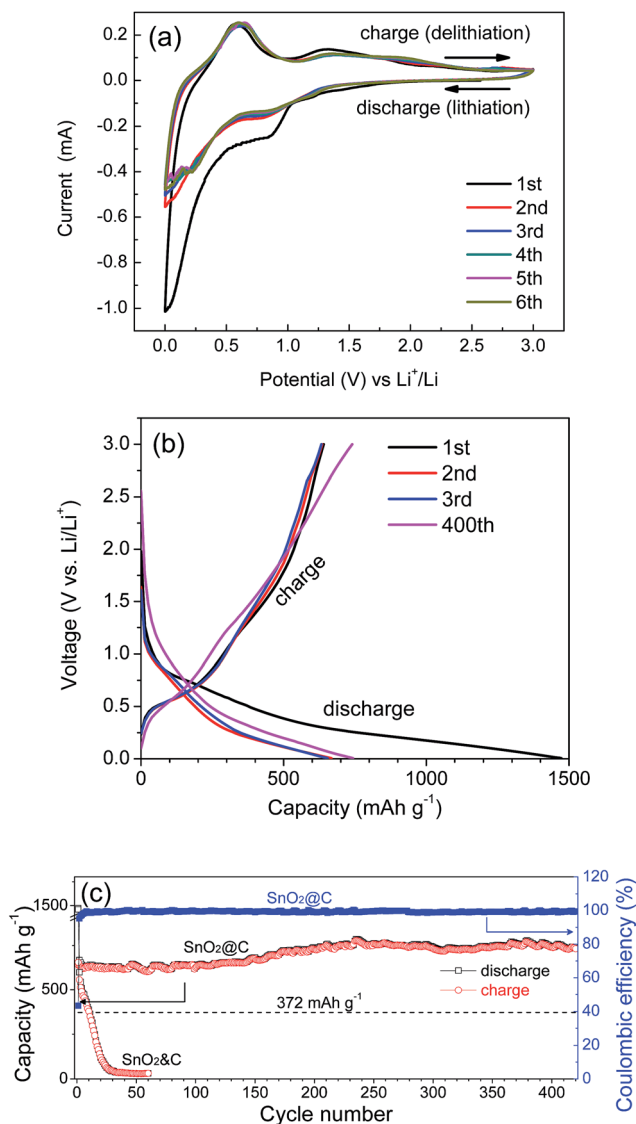


Fig. 5 (a) Cyclic voltammetry curves of the $\text{SnO}_2\text{@C}$ porous composite electrode at 0.1 mV s^{-1} scanning rate. (b) Galvanostatic charge–discharge profiles of the $\text{SnO}_2\text{@C}$ electrode at a constant current density of 500 mA g^{-1} . (c) Cycling performance of as-synthesized $\text{SnO}_2\text{@C}$ and commercial nano- SnO_2 with C mixture (SnO_2 & C) electrodes at 500 mA g^{-1} .

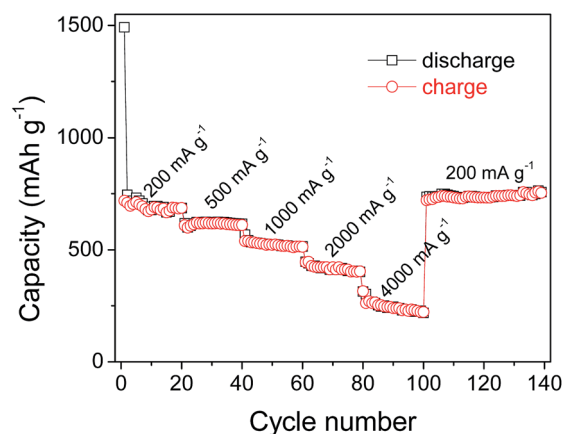


Fig. 6 Rate capability of the $\text{SnO}_2\text{@C}$ porous composite at different current densities.

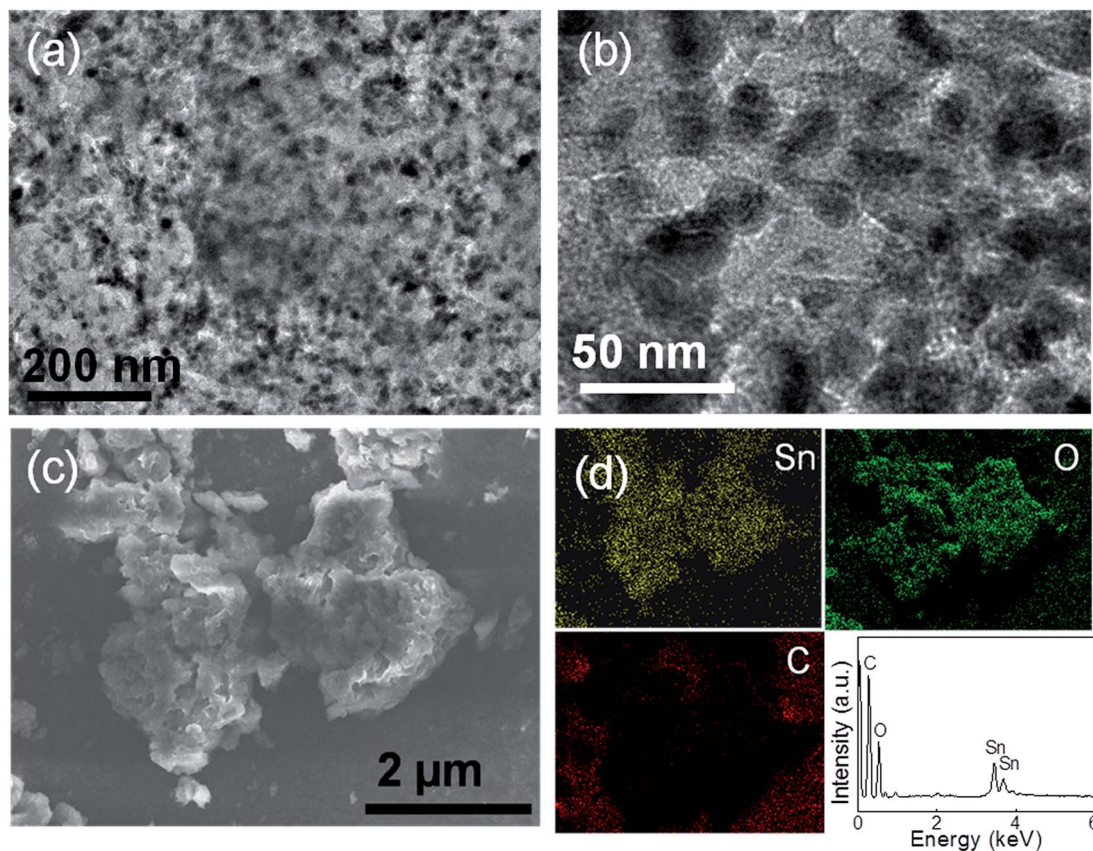


Fig. 7 TEM (a and b) and SEM (c) images of the SnO₂@C porous composite after the 100th electrochemical cycle. (d) is the EDS mapping results of the (c) image. The tremendous carbon signals outside the sample are derived from the carbon tape.

reported SnO₂/C composites.⁷ Remarkably, when the current rate is reduced back to 200 mA g⁻¹ after more than 100 cycles, the initial capacity is completely recovered.

The excellent cycling stability and rate capability of the SnO₂@C porous electrode might be attributed to the unique nanoporous structure of micro-sized SnO₂@C. Specifically, the primary island-like SnO₂ nanoparticles possess a short distance for Li⁺ ion diffusion and a large electrode–electrolyte contact area for high Li⁺ ion flux across the interface, leading to the enhanced rate capability.^{15,59} The carbon sheets can sufficiently act as the electron conducting channels during lithiation/delithiation processes and prevent the aggregation of Sn nanoparticles. Meanwhile, the local empty space around the SnO₂ nanoparticles associated with the carbon sheets can effectively accommodate the large volume change, thus leading to improved lithium-storage properties. The highly uniform nanoSnO₂@C morphologic aspect allows full utilization of SnO₂ nanoparticles to react with lithium ions, thus providing high capacity and improving the cycling stability. It is worth mentioning that the capacity retention of the SnO₂@C porous composite is significantly enhanced when compared with many other SnO₂ composites^{59–61} due to the unique structure of uniform dispersion of carbon coated SnO₂ nanoparticles in the micro-sized porous carbon matrix.

The structural and morphological changes of the SnO₂@C nanoporous composite after 100 cycles were investigated using TEM, SEM and EDS analyses. Fig. 7a and b present TEM images of the SnO₂@C porous composite after the 100th lithiation/delithiation cycle. No pulverization and agglomeration of the material are observed, which can explain the excellent cycling stability of the SnO₂@C porous composite. Fig. 7d shows the elemental mapping results of Fig. 7c for the distribution of Sn, O and C elements on the composite. As can be seen, the Sn and O signals are much stronger than that of C in the composite. In addition, the elemental mapping clearly indicates homogeneously dispersed Sn, O and C. This homogeneity implies a highly dispersed Sn distribution without any detectable aggregation, which will be favorable for lithiation/delithiation processes. The large amount of C outside the composite is derived from the double sided carbon tape which was used for SEM measurements.

Conclusions

In summary, we have synthesized a hierarchical SnO₂@C composite with carbon coated SnO₂ nanoparticles uniformly dispersed in the micro-sized porous carbon matrix using a facile and scalable solution–evaporation–calcination method.

The SnO₂@C nanoporous composite can provide a capacity of 420 mA h g⁻¹ at 2000 mA g⁻¹ and maintain 720 mA h g⁻¹ at 500 mA g⁻¹ for 420 cycles. The exceptional performance is attributed to the unique SnO₂/C nanoporous structure, where the uniformly dispersed carbon coated SnO₂ nanoparticles in the porous carbon matrix can (1) increase the electronic and ionic transport in the electrode, (2) effectively accommodate the volume variations of SnO₂ during lithiation/delithiation, and (3) prevent Sn nanoparticles from aggregation, thus providing high rate performance and cycling stability. Combining a simple and scalable synthesis method with excellent electrochemical performance, the present strategy makes the SnO₂@C porous composite a promising anode material for LIBs.

Acknowledgements

The authors gratefully acknowledge the support of the Program for Innovative Research Team in University of Ministry of Education of China (IRT13037), the Key Science and Technology Innovation Team of Zhejiang Province (2010R50013), the China Postdoctoral Science Foundation (2012M521167) and the International Postdoctoral Exchange Program (2013).

Notes and references

- 1 R. V. Noorden, *Nature*, 2014, **507**, 26–28.
- 2 J. M. Tarascon and M. Armand, *Nature*, 2001, **414**, 359–367.
- 3 B. Dunn, H. Kamath and J. M. Tarascon, *Science*, 2011, **334**, 928–935.
- 4 W. Ni, Y. Wang and R. Xu, *Part. Part. Syst. Charact.*, 2013, **30**, 873–880.
- 5 N. Nitta and G. Yushin, *Part. Part. Syst. Charact.*, 2014, **31**, 317–336.
- 6 Y. X. Yin, S. Xin and Y. G. Guo, *Part. Part. Syst. Charact.*, 2013, **30**, 737–753.
- 7 J. S. Chen and X. W. Lou, *Small*, 2013, **9**, 1877–1893.
- 8 J. S. Chen, L. A. Archer and X. W. Lou, *J. Mater. Chem.*, 2011, **21**, 9912–9924.
- 9 J. Zhu, J. Jiang, Y. Feng, G. Meng, H. Ding and X. Huang, *ACS Appl. Mater. Interfaces*, 2013, **5**, 2634–2640.
- 10 Y. J. Hong, M. Y. Son and Y. C. Kang, *Adv. Mater.*, 2013, **25**, 2279–2283.
- 11 X. W. Lou, Y. Wang, C. Yuan, J. Y. Lee and L. A. Archer, *Adv. Mater.*, 2006, **18**, 2325–2329.
- 12 C. Kim, M. Noh, M. Choi, J. Cho and B. Park, *Chem. Mater.*, 2005, **17**, 3297–3301.
- 13 S. Yoo, J. I. Lee, M. Shin and S. Park, *ChemSusChem*, 2013, **6**, 1153–1157.
- 14 V. Aravindan, K. B. Jinesh, R. R. Prabhakar, V. S. Kale and S. Madhavi, *Nano Energy*, 2013, **2**, 720–725.
- 15 L. Zhang, G. Zhang, H. B. Wu, L. Yu and X. W. Lou, *Adv. Mater.*, 2013, **25**, 2589–2593.
- 16 P. Wu, N. Du, H. Zhang, C. Zhai and D. Yang, *ACS Appl. Mater. Interfaces*, 2011, **3**, 1946–1952.
- 17 R. Yang, W. Zhao, J. Zheng, X. Zhang and X. Li, *J. Phys. Chem. C*, 2010, **114**, 20272–20276.
- 18 X. W. Lou, C. M. Li and L. A. Archer, *Adv. Mater.*, 2009, **21**, 2536–2539.
- 19 S.-M. Paek, E. Yoo and I. Honma, *Nano Lett.*, 2008, **9**, 72–75.
- 20 S. Li, Y. Wang, C. Lai, J. Qiu, M. Ling, W. N. Martens, H. Zhao and S. Zhang, *J. Mater. Chem. A*, 2014, **2**, 10211–10217.
- 21 Y. Huang, D. Wu, S. Han, S. Li, L. Xiao, F. Zhang and X. Feng, *ChemSusChem*, 2013, **6**, 1510–1515.
- 22 H. Song, N. Li, H. Cui and C. Wang, *J. Mater. Chem. A*, 2013, **1**, 7558–7562.
- 23 J. Lin, Z. Peng, C. Xiang, G. Ruan, Z. Yan, D. Natelson and J. M. Tour, *ACS Nano*, 2013, **7**, 6001–6006.
- 24 S. J. R. Prabakar, Y. H. Hwang, E. G. Bae, S. Shim, D. Kim, M. S. Lah, K. S. Sohn and M. Pyo, *Adv. Mater.*, 2013, **25**, 3307–3312.
- 25 X. Zhou, L. J. Wan and Y. G. Guo, *Adv. Mater.*, 2013, **25**, 2152–2157.
- 26 Y. Chen, B. Song, R. M. Chen, L. Lu and J. Xue, *J. Mater. Chem. A*, 2014, **2**, 5688–5695.
- 27 X. Liu, M. Wu, M. Li, X. Pan, J. Chen and X. Bao, *J. Mater. Chem. A*, 2013, **1**, 9527–9535.
- 28 Y. Li, S. Zhu, Q. Liu, J. Gu, Z. Guo, Z. Chen, C. Feng, D. Zhang and W. J. Moon, *J. Mater. Chem.*, 2012, **22**, 2766–2773.
- 29 Z. Chen, M. Zhou, Y. Cao, X. Ai, H. Yang and J. Liu, *Adv. Energy Mater.*, 2012, **2**, 95–102.
- 30 J. Zhu, G. Zhang, X. Yu, Q. Li, B. Lu and Z. Xu, *Nano Energy*, 2014, **3**, 80–87.
- 31 A. Bhaskar, M. Deepa, M. Ramakrishna and T. N. Rao, *J. Phys. Chem. C*, 2014, **118**, 7296–7306.
- 32 X. Li, X. Meng, J. Liu, D. Geng, Y. Zhang, M. N. Banis, Y. Li, J. Yang, R. Li, X. Sun, M. Cai and M. W. Verbrugge, *Adv. Funct. Mater.*, 2012, **22**, 1647–1654.
- 33 X. Wang, X. Cao, L. Bourgeois, H. Guan, S. Chen, Y. Zhong, D.-M. Tang, H. Li, T. Zhai, L. Li, Y. Bando and D. Golberg, *Adv. Funct. Mater.*, 2012, **22**, 2682–2690.
- 34 M. Zhang, Y. Li, E. Uchaker, S. Candelaria, L. Shen, T. Wang and G. Cao, *Nano Energy*, 2013, **2**, 769–778.
- 35 A. Jahel, C. M. Ghimbeu, L. Monconduit and C. Vix-Guterl, *Adv. Energy Mater.*, 2014, DOI: 10.1002/aenm.201400025.
- 36 L. Zhang, H. B. Wu and X. W. Lou, *Mater. Horiz.*, 2014, **1**, 133–138.
- 37 J.-M. Jeong, B. G. Choi, S. C. Lee, K. G. Lee, S. J. Chang, Y. K. Han, Y. B. Lee, H. U. Lee, S. Kwon, G. Lee, C. S. Lee and Y. S. Huh, *Adv. Mater.*, 2013, **25**, 6250–6255.
- 38 Y. Xu, J. Guo and C. Wang, *J. Mater. Chem.*, 2012, **22**, 9562–9567.
- 39 L. Ji, Z. Lin, M. Alcoutlabi and X. Zhang, *Energy Environ. Sci.*, 2011, **4**, 2682–2699.
- 40 Z. S. Wu, G. M. Zhou, L. C. Yin, W. Ren, F. Li and H. M. Cheng, *Nano Energy*, 2012, **1**, 107–131.
- 41 M. Zhang, D. Lei, Z. Du, X. Yin, L. Chen, Q. Li, Y. Wang and T. Wang, *J. Mater. Chem.*, 2011, **21**, 1673–1676.
- 42 J. Y. Huang, L. Zhong, C. M. Wang, J. P. Sullivan, W. Xu, L. Q. Zhang, S. X. Mao, N. S. Hudak, X. H. Liu, A. Subramanian, H. Fan, L. Qi, A. Kushima and J. Li, *Science*, 2010, **330**, 1515–1520.
- 43 C. He, S. Wu, N. Zhao, C. Shi, E. Liu and J. Li, *ACS Nano*, 2013, **7**, 4459–4469.

- 44 L. S. Zhang, L. Y. Jiang, H. J. Yan, W. D. Wang, W. Wang, W. G. Song, Y. G. Guo and L. J. Wan, *J. Mater. Chem.*, 2010, **20**, 5462–5467.
- 45 C. D. Wagner, W. M. Riggs, L. E. Moulder and G. E. Muilenberg, *Handbook of X-ray Photoelectron Spectroscopy*, Perkin-Elmer Corporation, 1979, p. 188.
- 46 J. Parmentier, S. Saadhallah, M. Reda, P. Gibot, M. Roux, L. Vidal, C. Vix-Guterl and J. Patarin, *J. Phys. Chem. Solids*, 2004, **65**, 139–146.
- 47 I. A. Courtney and J. R. Dahn, *J. Electrochem. Soc.*, 1997, **144**, 2045–2052.
- 48 M. S. Park, G. X. Wang, Y. M. Kang, D. Wexler, S. X. Dou and H. K. Liu, *Angew. Chem., Int. Ed.*, 2007, **46**, 750–753.
- 49 B. Luo, B. Wang, X. Li, Y. Jia, M. Liang and L. Zhi, *Adv. Mater.*, 2012, **24**, 3538–3543.
- 50 X. W. Lou, J. S. Chen, P. Chen and L. A. Archer, *Chem. Mater.*, 2009, **21**, 2868–2874.
- 51 Z. Wen, Q. Wang, Q. Zhang and J. Li, *Adv. Funct. Mater.*, 2007, **17**, 2772–2778.
- 52 N. Zhang, Q. Zhao, X. Han, J. Yang and J. Chen, *Nanoscale*, 2014, **6**, 2827–2832.
- 53 D. Wang, J. Yang, X. Li, D. Geng, R. Li, M. Cai, T. K. Sham and X. Sun, *Energy Environ. Sci.*, 2013, **6**, 2900–2906.
- 54 W. Wei, S. Yang, H. Zhou, I. Lieberwirth, X. Feng and K. Müllen, *Adv. Mater.*, 2013, **25**, 2909–2914.
- 55 Y. Jiang, D. Zhang, Y. Li, T. Yuan, N. Bahlawane, C. Liang, W. Sun, Y. Lu and M. Yan, *Nano Energy*, 2014, **4**, 23–30.
- 56 Y.-Y. Hu, Z. Liu, K. W. Nam, O. J. Borkiewicz, J. Cheng, X. Hua, M. T. Dunstan, X. Yu, K. M. Wiaderek, L. S. Du, K. W. Chapman, P. J. Chupas, X. Q. Yang and C. P. Grey, *Nat. Mater.*, 2013, **12**, 1130–1136.
- 57 J. S. Chen, Y. L. Cheah, Y. T. Chen, N. Jayaprakash, S. Madhavi, Y. H. Yang and X. W. Lou, *J. Phys. Chem. C*, 2009, **113**, 20504–20508.
- 58 M. S. Park, Y. M. Kang, S. X. Dou and H. K. Liu, *J. Phys. Chem. C*, 2008, **112**, 11286–11289.
- 59 C. Wang, Y. Zhou, M. Ge, X. Xu, Z. Zhang and J. Z. Jiang, *J. Am. Chem. Soc.*, 2009, **132**, 46–47.
- 60 W. Wang, P. Li, Y. Fu and X. Ma, *J. Power Sources*, 2013, **238**, 464–468.
- 61 X. Zhang, J. Liang, G. Gao, S. Ding, Z. Yang, W. Yu and B. Q. Li, *Electrochim. Acta*, 2013, **98**, 263–267.